



In-situ topotactic synthesis and photocatalytic activity of plate-like BiOCl/2D networks Bi₂S₃ heterostructures

Yiqiu Shi, Xuyang Xiong, Shuoping Ding, Xiufan Liu, Qingqing Jiang, Juncheng Hu*

Key Laboratory of Catalysis and Materials Science of the State Ethnic Affairs Commission & Ministry of Education, South-Central University for Nationalities, Wuhan, 430074, PR China



ARTICLE INFO

Keywords:
BiOCl/Bi₂S₃
Heterostructure
Hydrothermal method
Selective ion-exchange
Photocatalysis

ABSTRACT

We herein demonstrate the uniform porous hierarchical plate-like BiOCl/2D networks Bi₂S₃ heterostructures realized by a facile two-step hydrothermal technique. The synthesis involved an anion exchange process by reacting pre-synthesized BiOCl irregular octagonal nanoplates with Na₂S₂O₃·5H₂O in an aqueous solution. The experiment results revealed that the 3D plate-like heterostructures were composed of internal BiOCl and outside networks interwoven by 1D Bi₂S₃ nanorods. Interestingly, the heterostructures had almost the same thickness and the bigger length compared to the precursor BiOCl. We proposed the possible formation mechanism of the composites which involved selective ion-exchange reaction, the following Ostwald ripening process and epitaxial growth. And the crystal lattice matching between the a- or b-axis of tetragonal BiOCl ($a = b = 3.89 \text{ \AA}$) and the a-axis of orthorhombic Bi₂S₃ ($a = 3.981 \text{ \AA}$) could be responsible for the in-situ topotactic transformation. Due to the formation of hetero-nanostructures, the unique spatial architecture features and the existence of oxygen vacancies, the BiOCl/Bi₂S₃ composites exhibited significantly extended photo-responsive range and improved photocatalytic activity for reduction of Cr^{VI} under visible-light irradiation. Moreover, the possible mechanism of photocatalysis process was investigated. Our work is expected to inspire further attempts for hierarchical and unconventional hetero-nanostructures with unique spatial architecture, which is very promising for photocatalysis and other applications.

1. Introduction

Many novel applications of nanomaterials in solar cells [1], photonic and optoelectronic devices [2], photocatalysis [3], and bionanotechnology [4] are driving the exploration and development of the techniques to design and synthesize their chemical compositions, structures, and morphologies [5–7]. Three-dimensional (3D) nanomaterials, which usually possess distinctive spatial architecture features, have been attracting great attention [8–10]. Up to now, there have been increasing attempts and successes in the preparation of 3D nanostructures. Firstly, 3D nanostructures were based on zero-dimensional (0D) nanoparticles, such as the Te plates composed of 0D Te nanoparticles obtained by two-step method [11]. Secondly, 3D nanomaterials were synthesized using the one-dimensional (1D) nanorods or nanowires. N-Si/n-TiO₂ core/shell nanowire arrays were synthesized from 0D TiO₂ by growth on their surfaces of 1D Si electroless etched nanowire arrays [12]. Hyperbranched nanowires were prepared by gold nanoclusters deposition on Si nanowires [13]. Homo- and heterobranched nanowires were obtained by the secondary growth of 1D

nanowires [14]. The third kind of 3D nanostructures were based on the 2D precursors. The following growth of nanowires on the 2D nanoplates can be realized to obtain complex 3D nanostructures [15]. Fourthly, 3D nanomaterials were gained by treating 3D precursors with ion-exchange or the Kirkendall effect methods. S²⁻ ions are introduced into pre-synthesized 3D BiVO₄ discoid-like particles to form 3D hollow mesoporous heterostructures by a facile ion-exchange method [16].

Hetero-nanostructures, which always possess staggered array of band edges at the interface [17,18] and mesoporous structures or hollow interiors [16,19,20], are usually considered to be of great potential for various applications due to their enhanced or new physicochemical properties. It is worth noting that there are some 3D heterostructures taking advantages of both 1D and 2D compositions, geometries. 1D nanorods grew selectively on the pre-synthesized 2D nanoplates to form hierarchical 1D/2D heterostructures [15,21,22]. However, the rational design and synthesis of hierarchical 3D heterostructures with distinctive architecture and performances remain a great challenge. The obstacles come from combining the existence of interfaces, different growth modes and the incompatibility, which

* Corresponding author.

E-mail address: jchu@mail.scuec.edu.cn (J. Hu).

usually results in uniformity and poor structural stability [16].

Among Bi-based semiconductor materials, BiOCl, characterized by $[Bi_2O_2]$ slabs interleaved by double layers of Cl atoms, is promising for many applications in pigments, photocatalysis, catalysts, as well as storage materials due to the unique layered structure and excellent optical and electrical properties [23,24]. However, BiOCl has an indirect wide band gap ($E_g = 3.2\text{--}3.6\text{ eV}$) and limited absorbance of UV light, which prevent its further applications. To overcome these obstacles, some effective strategies were studied, such as controlling exposed crystal facets, varying morphology and size, ion or metal doping, as well as creating heterostructures. Zhang et al. found that BiOCl nanosheets with exposed {001} and {010} facets showed different activities for pollutant degradation [25]. Our lab reported the porous BiOCl hexagonal prisms for the first time [26]. Xiong et al. synthesized Ag/Pd/BiOCl which showed improved photocatalytic performance by synergistically utilizing Schottky-junction and plasmonic effect [27]. BiOCl-based heterostructures, such as Co_3O_4 /BiOCl [28], In_2O_3 /BiOCl [29], TiO_2 /BiOCl [30], BiOCl/ZnO [31], exhibited enhanced performance compared to their individual ones. Among these methods, creating heterostructures is more flexible and interesting.

As a metal sulfide with a layer structure, Bi_2S_3 , with a direct narrow band gap of 1.3–1.7 eV, is of great potential for applications, such as lithium ion batteries [32], electrochemical hydrogen Storage [33], visible-wavelength photodetectors [34] and so on. Though Bi_2S_3 has good visible light response, it is hindered for applications due to the rapid photogenerated electron–hole recombination [35]. Doping and creating heterostructures are the effective methods to achieve electron–hole pair effective separation. Our lab synthesized Sn doped Bi_2S_3 microspheres which showed improved photocatalytic activity for RhB degradation [36]. The Bi_2S_3 –ZnO heterostructure nanosheets exhibited higher activity than pure ZnO and Bi_2S_3 [35]. There are some works in the preparation of Bi_2S_3 /BiOCl [37–41] with enhanced photocatalytic performance through in-situ etching, one-pot approach at room temperature, biomolecule-assisted solvothermal method and ion-exchange method. Although synthesizing heterostructured materials is a big challenge, it still receives increasing attention. The formation of heterostructure between two semiconductors may endow the material with excellent performance due to the extended photoresponse range and improved separation efficiency of e–h pairs.

Herein, we report the uniform, porous and hierarchical BiOCl/2D networks Bi_2S_3 heterostructures synthesized by a facile two-step hydrothermal method. The strategy involved a facile anion-exchange process by treating uniform BiOCl irregular octagonal nanoplates with $Na_2S_2O_3 \cdot 5H_2O$ in an aqueous solution to perform a hydrothermal process. We tuned the content of Bi_2S_3 phase in the hybrids by controlling the concentration of $Na_2S_2O_3 \cdot 5H_2O$ in the reaction system. The possible formation mechanism of the composites was investigated by characterizing the samples obtained after the time-dependent reactions. The crystal lattice matching between the a- or b-axis of tetragonal BiOCl ($a = b = 3.89\text{ \AA}$) and the a-axis of orthorhombic Bi_2S_3 ($a = 3.981\text{ \AA}$) could be responsible for the topotactic transformation from BiOCl nanoplates to BiOCl/ Bi_2S_3 . Benefiting from the formation of heterostructures, the unique spatial architecture and the oxygen vacancies, the BiOCl/ Bi_2S_3 heterostructures exhibited significantly enhanced optical properties and photocatalytic activity for reduction of Cr^{VI} under visible-light illumination. This work provides insight into the formation mechanism of BiOCl/ Bi_2S_3 , and is expected to inspire further attempts for well-designed and unconventional hetero-nanostructures with shape-dependent enhanced performances.

2. Experimental

2.1. Materials

Bismuth nitrate pentahydrate [$Bi(NO_3)_3 \cdot 5H_2O$], sodium chloride [$NaCl$], sodium thiosulfate pentahydrate [$Na_2S_2O_3 \cdot 5H_2O$], nitric acid

[HNO_3], potassium dichromate [$K_2Cr_2O_7$] were purchased from Sinopharm Chemical Reagent Co., Ltd. (Shanghai, China). Chitosan was purchased from Aladdin Chemistry Co., Ltd (Shanghai, China). All of the reagents were analytical grade and used as received without any further purification.

2.2. Preparation of BiOCl irregular octagonal nanoplates

BiOCl irregular polygonal nanoplates were prepared in advanced. In a typical synthetic process, 5 mmol $Bi(NO_3)_3 \cdot 5H_2O$ was put into a 50 mL beaker which contained the mixed solution of 19 mL deionized water and 1 mL nitric acid. The mixture was stirred and sonicated until $Bi(NO_3)_3 \cdot 5H_2O$ was dissolved absolutely and labeled as solution A. Simultaneously, 5 mmol $NaCl$ was dissolved into 5 mL deionized water, followed by addition of 40 mL 10 g L^{-1} aqueous solution of Chitosan, resulting in a transparent solution B. Subsequently, solution A was slowly added to solution B in drops with continuous stirring and sonication. Then, the mixture was transferred into a 100 mL Teflon-lined stainless steel autoclave, which was subsequently placed in an oven at 180°C for 6 h. When cooling down to ambient temperature naturally, the obtained white precipitates were collected by filtered and washed with deionized water and ethanol for several times to thoroughly remove residual ions, and finally dried at 60°C in air for 12 h for further use.

2.3. Preparation of uniform porous hierarchical BiOCl/2D networks Bi_2S_3 heterostructures

BiOCl/ Bi_2S_3 was synthesized though a hydrothermal method. The pre-synthesized BiOCl (2 mmol) was dispersed in 20 mL deionized water and magnetically stirred for 20 min. Afterwards, 20 mL sodium thiosulfate pentahydrate ($Na_2S_2O_3 \cdot 5H_2O$) aqueous solution was added into the suspension, followed by magnetically stirring for 20 min. The mixture was transferred to a 100 mL Teflon-lined stainless steel autoclave to perform the hydrothermal process at 180°C for 6 h. After cooling down to ambient temperature naturally, the resulting precipitates were collected by filtered and washed with deionized water and ethanol for several times to remove the residual impurities, and finally dried at 60°C in air for 12 h for further characterization. To investigate the effect of $Na_2S_2O_3 \cdot 5H_2O$ concentration on the formation of BiOCl/ Bi_2S_3 hetero-nanostructures, $Na_2S_2O_3 \cdot 5H_2O$ solutions with different concentrations (0.025, 2, 4 and 6 mmol) were used in the anion exchange process, while keeping other conditions unchanged. The samples were designated as H-1, H-2, H-3 and H-4, respectively. To observe the growth process of BiOCl/ Bi_2S_3 composites, we carried out the time-dependent reactions. The 4 mmol $Na_2S_2O_3 \cdot 5H_2O$ solutions was used to perform the anion exchange process for 20 min, 40 min, 1 h, 2 h, 4 h, 6 h, 12 h, 24 h and 48 h under otherwise identical conditions.

2.4. Characterization

The powder X-ray diffraction (XRD) (Bruker D8 Advance; $Cu K\alpha = 1.5404\text{ \AA}$) was employed to study the crystalline structure of the prepared samples. The 2θ range was from 10° to 80° with a scanning rate of $0.05^\circ/\text{s}$. The microstructure and size of the samples were investigated by a SU8010 field-emission scanning electron microscope (FESEM, Hitachi, Japan) at a decelerating voltage 2 KV. Energy dispersive spectrum (EDS) was connected to the SEM. Transmission electron microscope (TEM) and high resolution transmission electron microscopy (HRTEM) were obtained on a Tecnai G20 (FEI Co., Holland) microscope operated at an accelerating voltage of 200 kV, the sample powder was dispersed into ethanol by ultrasonic treatment and dropped a very dilute suspension onto a copper grid. X-ray photoelectron spectroscopy (XPS) was recorded on a VG Multilab 2000 (VG Inc.) photoelectron spectrometer using monochromatic $Al K\alpha$ radiation as the excitation source under vacuum at $2 \times 10^{-6}\text{ Pa}$. All the binding

energies were referenced to the C 1 s peak at 284.8 eV of the surface adventitious carbon. The Brunauer-Emmett-Teller (BET) specific surface areas of the samples were evaluated through the nitrogen adsorption and desorption isotherms using a Micromeritics ASAP 2020 gas adsorption apparatus (USA). The UV-vis diffused reflectance spectra (DRS) were tested with a Cary Series UV-vis-NIR Spectrophotometer (Agilent Technologies) from 200 to 1500 nm by a diffuse reflectance method using polytetrafluoroethylene as a reference materials. Photoluminescence (PL) measurements were carried out at room temperature in a Hitachi F-7000 with a 150 W Xe lamp. The samples were excited at 240 nm, and the emission filter (300–800 nm) was used to minimize the background single at the excitation wavelength. The electron spin resonance (ESR) measurement were carried out in dark by using a JES FA-200 spectrometer (JEOL, Japan) equipped dual cavity with modulation and microwave frequencies of 100 kHz and 9.4145 GHz, respectively. The 2,2,6,6-Tetramethylpiperidinoxy (TEMPO) were used as the spin-trapped reagent. The g-factors were determined by the ESR Data Processing program. Electrochemical impedance spectra (EIS) was performed by an electrochemical system (CHI-660e, CHI Shanghai, Inc.) in three-electrode quartz cells with 0.5 M Na₂SO₄ electrolyte solution, and platinum wire was used as the counter electrode, saturated calomel electrodes (SCE) were used as the reference electrodes, samples coated on ITO were used as the working electrodes, respectively. The tests were performed at a 1.6 mV of alternating current signal in the frequency range of 1–105 Hz and the data obtained were fitted using ZSimpWin software.

2.5. Photocatalytic activity evaluation

The photocatalytic activities of the phase-pure BiOCl and BiOCl/Bi₂S₃ heterostructures were evaluated by photocatalytic reduction of Cr(VI) under visible light illumination. The visible light was provided with a 350 W Xe lamp using an ultraviolet cutoff filter ($\lambda > 420$ nm). In a typical process, 50 mg of the as-prepared photocatalyst was added into 100 mL Pyrex glass bottle which contained 50 mL of Cr(VI) solution (10 mg L⁻¹ based on Cr in a dilute K₂Cr₂O₇ solution). Before irradiation, the suspensions were prepared under ultrasound for 10 min and magnetically stirred in the dark for 1 h to ensure the establishment of adsorption-desorption equilibrium. During the photoreaction, 4 mL of the suspension was removed from the reactor at given time intervals. The supernatant liquid was obtained after centrifugation for further analysis.

The diphenylcarbazide (DPC) method was used to determine the concentration of Cr(VI) ions in the supernatant solution obtained after photocatalytic experiment [42]. 1 mL of Cr(VI) solution obtained after photocatalytic reduction was mixed with 9 mL of 0.2 M H₂SO₄ aqueous solution in a 10 mL volumetric flask. Then, 0.2 mL of newly prepared 0.25% (w/v) diphenylcarbazide (DPC) in acetone was added to the volumetric flask. After vortexing the mixture for about 15–30 s, it was allowed to stand for 10–15 min so as to ensure full color development. The red-violet to purple color mixed solution was then measured at 540 nm with the UV-vis spectroscopy using deionized water as reference.

3. Results and discussion

3.1. Crystal structure and morphologies

The crystallographic structure and phase purity of the as-obtained samples were first examined by powder X-ray diffraction (XRD) analysis. All the diffraction peaks (Fig. 1a) can be indexed as the tetragonal crystallites of BiOCl with lattice constants of $a = b = 3.89$ Å and $c = 7.37$ Å (JCPDS card no. 85-0861). No other diffraction peaks were detected, indicating the high purity and single-phase of the samples. Interestingly, (001), (002) and (003) diffraction peaks of BiOCl are sharper and stronger than any other peaks, which means that the BiOCl

irregular octagonal nanoplates could be phase pure and prefer to grow along the c axis ([001] orientations) perpendicular to the platelets [33,43].

The BiOCl/Bi₂S₃ heterostructures are realized by a facile ion-exchange procedure under hydrothermal conditions using the BiOCl nanoplates as the precursor and Na₂S₂O₃·5H₂O as the sulfidation agent. The successful formation of BiOCl/Bi₂S₃ heterostructures is confirmed by XRD analysis. As shown in Fig. 1b, in addition to the diffraction peaks of BiOCl, other peaks can be well assigned to orthorhombic phase of Bi₂S₃ (JCPDS card no. 84-0279; $a = 3.981$ Å, $b = 11.147$ Å and $c = 11.305$ Å). Interestingly, with the increase of Na₂S₂O₃·5H₂O concentration, the diffraction intensity of the Bi₂S₃ phase becomes stronger, indicating the increasing content of Bi₂S₃ in the formed BiOCl/Bi₂S₃ heterostructures.

The morphology of the as-obtained phase-pure BiOCl was characterized by scanning electron microscopy (SEM). As shown in Fig. 2c, a panoramic SEM image shows that the BiOCl precursor consists of uniform irregular octagonal nanoplates with the average diameter of ca. 1.84 μm (Fig. S1b). The magnified SEM image (Fig. 2a) shows the top view of BiOCl, which further reveals that those nanoplates possess smooth surface with a concave center. From the side view of several arranged nanoplates in Fig. 2c, the thickness is estimated to be ca. 314 nm (Fig. S1a).

A representative sample of the as-prepared BiOCl/Bi₂S₃ heterostructures (sample H-3) was subjected to detailed characterizations. As shown in Fig. 2f, the panoramic SEM image shows that BiOCl/Bi₂S₃ is composed of uniform 3D nanoplates with the average diameter of ca. 2.22 μm (Fig. S1d), which is a little bigger than that of BiOCl nanoplates. As shown in Fig. 2d, there are obvious pore structure, and the amazing surface of the as-obtained heterostructures which consists of 2D networks. The networks are interwoven by crossed nanorods with a diameter of about 50 nm and the angle between the neighboring nanorods is about 90°. From the side view of BiOCl/Bi₂S₃ (Fig. 2e), the thickness is estimated to be ca. 313 nm (Fig. S1c), which is almost the same as that of BiOCl nanoplates. It is worth noting that the shape of the precursor BiOCl nanoplates is well preserved and the nanoplates are converted into porous heterostructures. Based on previous literature, Bi₂S₃ usually tends to a rod-based growth due to preferential growth of [001]-oriented [43,44]. We speculate that the 2D networks on the top facets of BiOCl/Bi₂S₃ heterostructures are interwoven by crossed Bi₂S₃ nanorods. These results show that the product well duplicates the thickness and shape of the precursor BiOCl nanoplates, and the solid BiOCl nanoplates are converted into porous heterostructures.

Chemical element mapping analysis (Fig. S2b–e) reveals that the elements including bismuth, oxygen, chlorine and sulfur are homogeneously distributed over the BiOCl/Bi₂S₃ heterostructures sample H-3. The SEM-EDS area scans (Fig. S2f) confirm the presence of Bi, O, Cl and S elements in the BiOCl/Bi₂S₃ heterostructures.

As shown in TEM image (Fig. 3a), the BiOCl is irregular octagonal nanoplates, which is consistent with the SEM results. A typical HRTEM image (Fig. 3b) exhibits the lattice spacing of 0.275 nm, which is indexed to the spacing between the {110} facets [43]. These observations illustrate that the BiOCl nanoplates obtained after the first hydrothermal process are principally composed of {001} facets, in conformity with the XRD data.

The crystalline structure of the BiOCl/Bi₂S₃ sample H-3 was further characterized by TEM and HRTEM. As shown in Fig. 3c, it can be observed that 2D networks are interwoven by crossed nanorods. The HRTEM images of ends of individual nanorods displayed in Fig. 3d, e and the corresponding FFT pattern (insert in Fig. 3d) exhibit clear lattice fringes and suggest the single-crystalline nature of the Bi₂S₃ nanorods. In Fig. 3f, the typical HRTEM image of the individual nanorod display the lattice spacing of about 0.352 nm, which is consistent with the spacing of (031) planes of orthorhombic Bi₂S₃. Although the fringes of the (100) facet are not found in the image, it can still be proposed that the nanorods grow along the [100] direction, which is

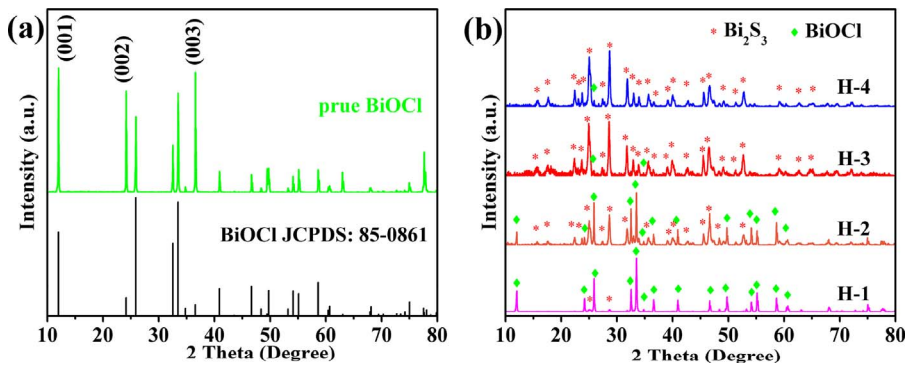
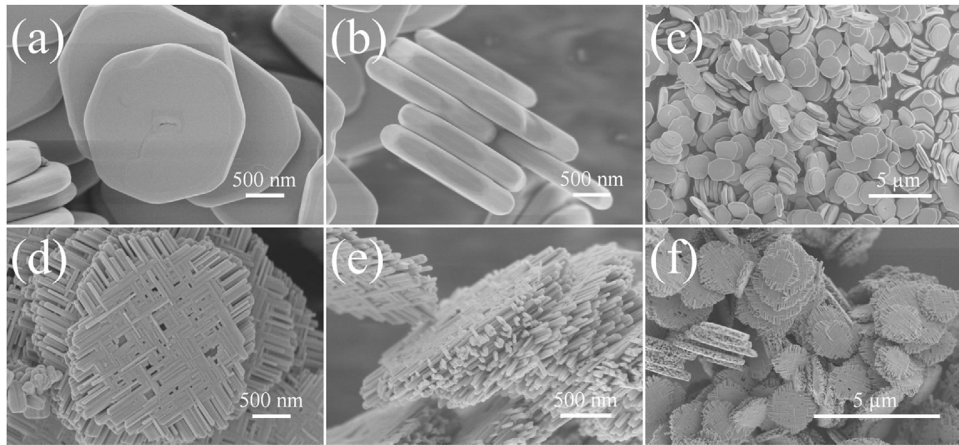


Fig. 1. XRD patterns of the samples: (a) pure BiOCl, (b) BiOCl/Bi₂S₃ heterostructures obtained with Na₂S₂O₃·5H₂O solutions of different concentrations.



perpendicular to (031) facets [44]. These observations indicate that each nanorod is a single-crystalline nanorod elongated along the [100] direction. In other words, the Bi₂S₃ nanorods elongate along the short axis (*a* axis) direction, which is accordant with the previous works [33,44–47]. We can conclude that the 2D networks on the top facets of BiOCl/Bi₂S₃ are interwoven by crossed Bi₂S₃ nanorods, which is consistent with our speculation.

The Brunauer–Emmett–Teller (BET) specific surface areas and the porous structure of BiOCl/Bi₂S₃ heterostructures (sample H-3) were investigated by nitrogen adsorption–desorption measurements. The N₂ adsorption–desorption isotherms (Fig. S3a) can be classified as type IV isotherm with a distinct hysteresis loop, which starts at P/P₀ = 0.4 and shows high adsorption at P/P₀ = 1.0, indicating the existence of abundant mesopores [48,49]. The BiOCl/Bi₂S₃ heterostructures (sample H-3) display a moderate Brunauer–Emmett–Teller (BET) specific surface area of about 451.5 m² g⁻¹. Meanwhile, the Barrett–Joyner–Halenda (BJH) pore size distribution curve of H-3 is depicted in Fig. S3b, exhibiting that the size of mesopores is centered around 8.2 nm. These mesoporous structure is in favor of improving the photocatalytic activity by facilitating the diffusion and adsorption of pollutants into the heterostructures.

3.2. Chemical compositions and valence state

Furthermore, the chemical compositions and valence state of various elements in the phase-pure BiOCl and the representative BiOCl/Bi₂S₃ sample (H-3) have been characterized by XPS spectra. As shown in Fig. 4, the two characteristic peaks at 164.8 and 159.5 eV belongs to Bi 4f_{5/2} and 4f_{7/2}, respectively, which are features of the Bi³⁺ in BiOCl. Other fitted peaks corresponding to O²⁻ (531.0 eV, O 1s in BiOCl; 530.1 eV, O 1s of components (OH and H₂O) absorbed on the BiOCl surface) and Cl⁻ (199.8 eV, Cl 2p_{1/2}; 198.2 eV, Cl 2p_{3/2}) could readily be detected from the XPS spectra [26]. This provides direct evidence

that the nanoplates are composed of BiOCl.

The high-resolution XPS spectra of the representative BiOCl/Bi₂S₃ sample (H-3) is depicted in Fig. 4. Two strong peaks centered at 163.5 and 158.2 eV can be attributed to the spin-orbit coupling effect of the Bi 4f_{5/2} and Bi 4f_{7/2}, respectively, which are the characteristics of Bi³⁺ in Bi₂S₃ [50]. The two characteristic peaks of Bi³⁺ 4f in BiOCl were not observed, the possible reason is the low content of BiOCl phase on surface of the BiOCl/Bi₂S₃ sample (H-3). Interestingly, a slight Bi³⁺ XPS peak shift to low binding energy in BiOCl/Bi₂S₃ sample can be observed compared with Bi³⁺ 4f_{5/2} (164.8 eV) and 4f_{7/2} (159.5 eV) in phase-pure BiOCl, which may be attributed to the variations of the chemical environment with the introduction of S²⁻ [50]. The O 1s (Fig. 4c) peaks could be fitted into two peaks, including a low-BE peak at 531.1 eV belonging to normal O in the crystal structure of BiOCl phase of BiOCl/Bi₂S₃ and a high-BE peak at 532.8 eV corresponding to O in oxygen-deficient regions (ODR) [51]. In addition, typical characteristic doublets of chloride anions (Fig. 4d) were too weak to be observed. The situation that the XPS characteristic peaks of Cl is very weak in BiOCl/Bi₂S₃ compared to that of phase-pure BiOCl, is similar to Bi and O in BiOCl phase of BiOCl/Bi₂S₃. This further reveals that there is little BiOCl phase on the surface of BiOCl/Bi₂S₃. The peak (161.2 eV) found between Bi 4f_{7/2} and Bi 4f_{5/2} (Fig. 4b) could be assigned to S 2p [52,53]. The S 2s peak (Fig. 4e) could be deconvoluted into two Gaussian peaks, including a lower energy peak at 225.5 eV consistent with a Bi-S species in Bi₂S₃ and a higher energy peak at 227.9 eV corresponding to S₈ [50,54].

Above XPS analysis results provided direct evidence that the obtained composites are composed of BiOCl and Bi₂S₃ and the heterostructures between BiOCl and Bi₂S₃ are formed. After the ion-exchange process, the O and Cl ions of BiOCl nanoplates was replaced by S ions and the porous BiOCl/Bi₂S₃ heterostructures were obtained. Combining with XRD, SEM and TEM results above-mentioned, we can further confirm that the 3D architecture of BiOCl/Bi₂S₃ composites is internal

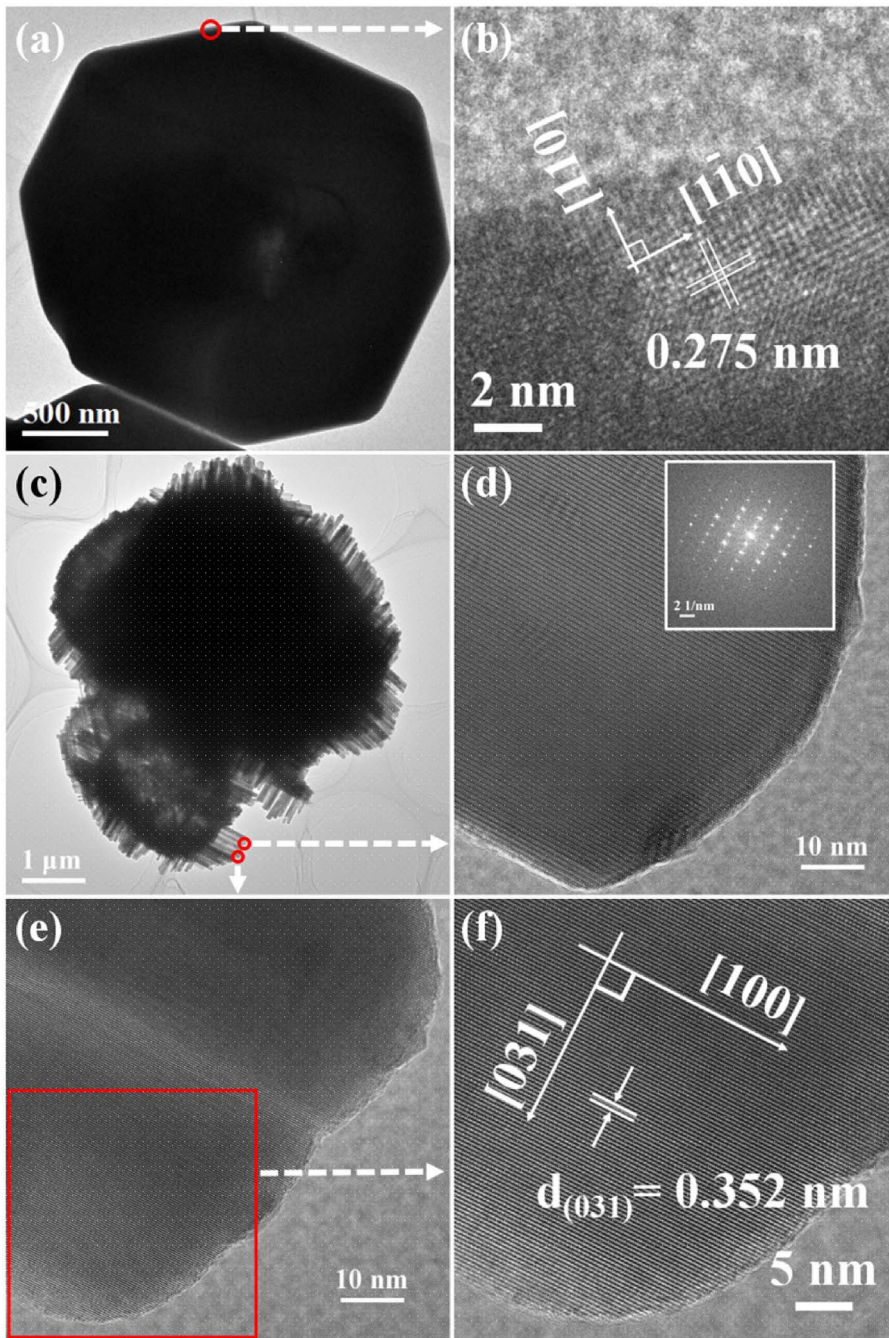


Fig. 3. TEM and HRTEM images of phase-pure BiOCl and BiOCl/Bi₂S₃ heterostructures (sample H-3): (a) the low-magnification TEM image and (b) the corresponding HRTEM image of BiOCl; (c) TEM, (d–f) HRTEM images of BiOCl/Bi₂S₃ sample H-3. The inset in (d) shows the corresponding FFT pattern.

BiOCl coated by 2D networks Bi₂S₃.

The higher energy O 1s peak located at 532.8 eV belongs to O in oxygen-deficient regions (ODR), indicating the existence of oxygen vacancies. The presence of oxygen vacancies was further confirmed by electron spin resonance (ESR) spectroscopy. As described at Fig. 4f, some oxygen vacancies generated in pure BiOCl after the hydrothermal process at the first step and became more after the ion-exchange reaction. The characteristic signal at a g-value (i.e., the spectral splitting factor) of 2.0026 is also detected, providing evidence of oxygen vacancies (OV) located at the surface of BiOCl/Bi₂S₃ sample (H-3) [51,55,56]. Oxygen vacancy, which serve as one kind of point defect, plays a very important role in the photocatalytic degradation reaction.

3.3. Possible formation mechanism of BiOCl/Bi₂S₃ heterostructures

To clarify the detailed formation mechanism of as-obtained

hierarchical BiOCl/Bi₂S₃ heterostructures, XRD, SEM, and EDS were used to characterize the morphologies and compositions of the products obtained at different reaction time. As depicted in the SEM image (Fig. 5a), no obvious change was observed after 20 min. When the exchange reaction of the BiOCl nanoplates with Na₂S₂O₃·5H₂O proceeding for 40 min, the edges of the nanoplates become rough and porous, while their middle parts are still smooth (Fig. 5b), indicating that the edges of the nanoplates are more reactive than the middle parts. The point-scan EDS spectra of the edge and the middle reveal that some oxygen ions and chloride ions in the edges of BiOCl nanoplates have been exchanged with sulfur ions (Fig. 7c and Table S1), while sulfur ions in the middle parts of the nanoplates are almost not observed (Fig. 7d and Table S2), confirming that the ion-exchange reaction is selective for the BiOCl nanoplates. The possible reason is that the density of O atoms on {001} facets of BiOCl (Fig. S4) is much higher than on other facets [55,25,57], which is not favorable for the

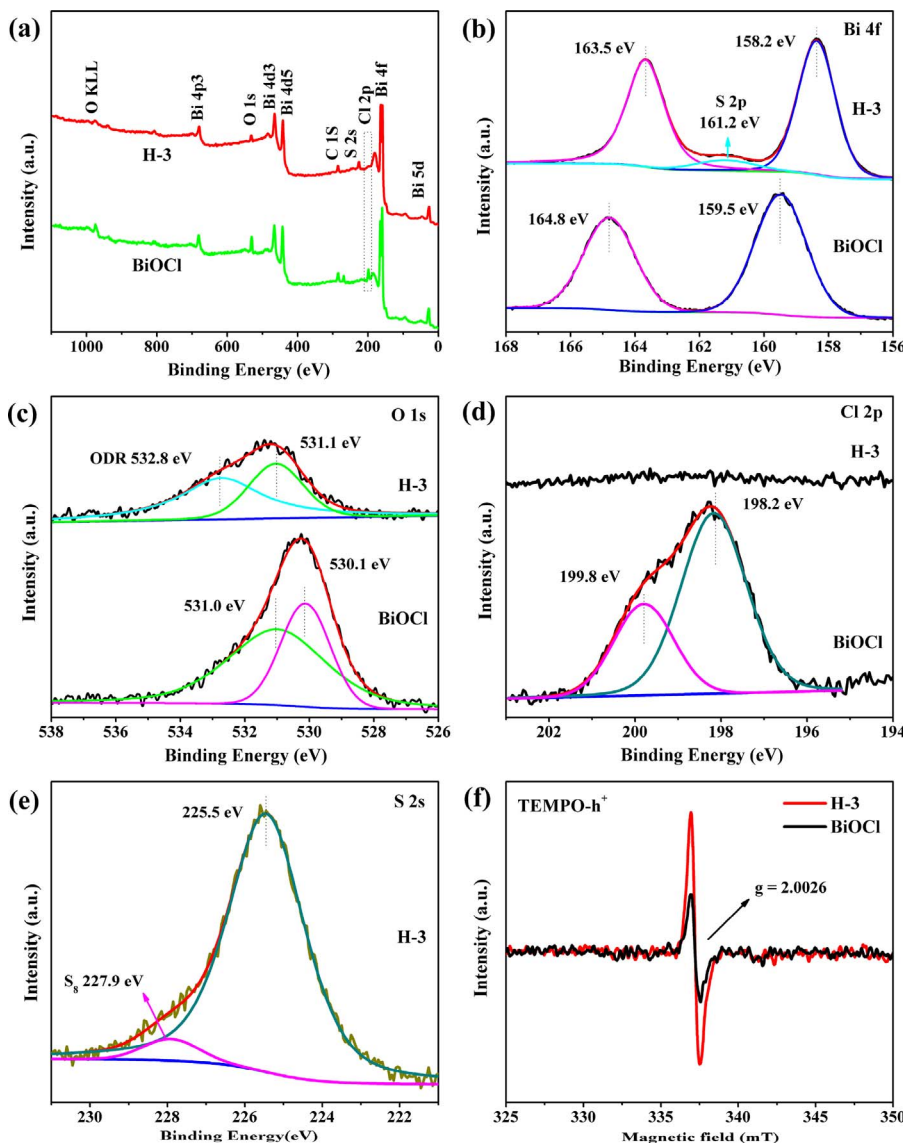


Fig. 4. XPS spectra of phase-pure BiOCl and BiOCl/Bi₂S₃ sample H-3: (a) survey scan, (b) Bi 4f, (c) Cl 2p, and (d) O 1s, (e) S 2s of H-3. (f) ESR spectra of sample H-3 and BiOCl.

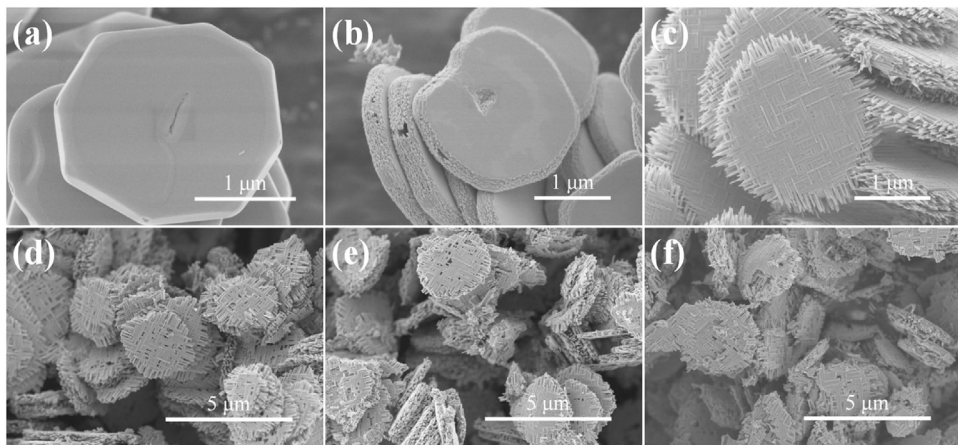


Fig. 5. SEM images of BiOCl/Bi₂S₃ obtained at different ion-exchange reaction times: (a) 20 min, (b) 40 min, (c) 1 h, (d) 12 h, (e) 24 h, (f) 48 h.

adsorption of the S²⁻ on the two sides of BiOCl. Another reason is the residual chitosan which attaches itself to BiOCl surfaces by hydrogen bonds between the hydroxyl of chitosan molecules and the exposed oxygen atoms in BiOCl (001) facets [58]. Thus the ion exchange on the surfaces is delayed compared with the ion exchange on the edges. When

the exchange reaction proceeded for one hours, Bi₂S₃ sticks were observed both on the surface and edges of the nanoplates (Fig. 5c). These observations coincided with the XRD results (Fig. 6), which showed that there were no Bi₂S₃ diffraction peaks for 40 min and obvious Bi₂S₃ diffraction peaks for 1 h. Bi₂S₃ sticks sizes became larger and obvious

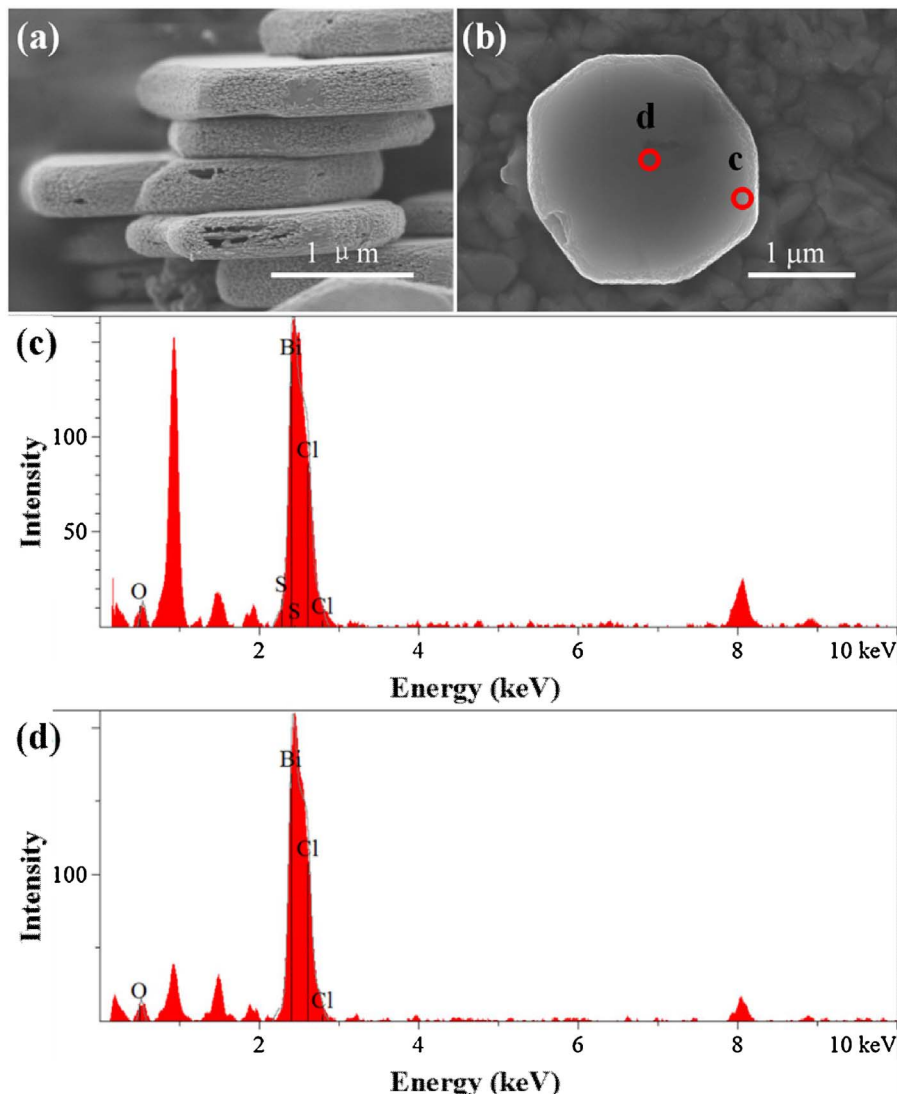


Fig. 7. SEM, point-scan EDS spectra of BiOCl/Bi₂S₃ obtained after ion-exchange for 40 min: (a) side view, (b) top view; the corresponding point-scan EDS spectra of (c) the edge and (d) the middle.

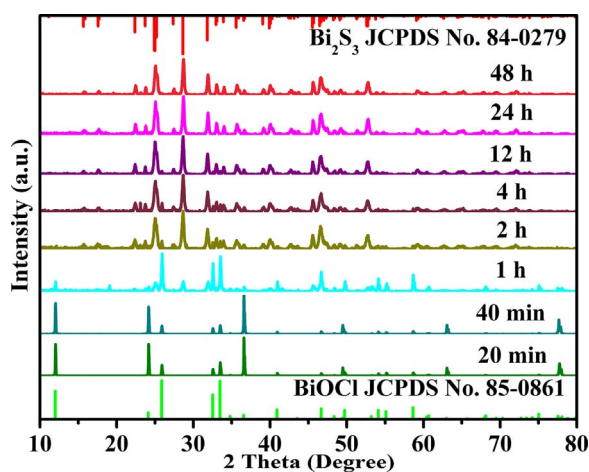


Fig. 6. XRD patterns of the samples obtained at different ion-exchange reaction time: 20 min, 40 min, 1 h, 2 h, 4 h, 12 h, 24 h, 48 h.

pore structure was obtained after 6 (Fig. 2b–d) and 12 (Fig. 5d) hours of exchange reaction, whose process included the typical Ostwald ripening mechanism.

The transformation of BiOCl into heterostructured BiOCl/Bi₂S₃ is

thermodynamically favored by reacting precursor BiOCl nanoplates with S²⁻ anions, due to the rather lower solubility of Bi₂S₃ ($K_{sp} = 1.0 \times 10^{-97}$) relative to BiOCl ($K_{sp} = 1.8 \times 10^{-31}$) [41]. According to the literatures [33,44–46], it may be inferred that the [001]-oriented Bi₂S₃ nanorods developed preferentially from the BiOCl along the two perpendicular, equivalent [100] and [010] directions due to the structural relationship between the c-axis of orthorhombic Bi₂S₃ ($c = 3.98 \text{ \AA}$) and the a- or b-axis of tetragonal BiOCl ($a = b = 3.89 \text{ \AA}$). Taking into consideration our results and the literatures, we proposed that the structural relationship between the a- or b-axis of tetragonal BiOCl ($a = b = 3.89 \text{ \AA}$) and the a-axis of orthorhombic Bi₂S₃ ($a = 3.981 \text{ \AA}$) could be responsible for the topotactic transformation from BiOCl irregular octagonal nanoplates to hierarchical 3D BiOCl/Bi₂S₃ heterostructures (Fig. S4). And the [100]-oriented single-crystalline Bi₂S₃ nanorods grew preferentially from the BiOCl nanoplates along the two perpendicular, equivalent [100] and [010] directions. (Fig. 8)

When the reaction proceeded for 24 h, the destruction of the architecture appeared (Fig. 5e). The more serious damage was detected at the prolonged exchange reaction for 48 h (Fig. 5f). The XRD patterns of the samples obtained at different reaction time in Fig. 6 revealed that the BiOCl nanoplates turned completely into Bi₂S₃ when the exchange reaction proceeded for 24 and 48 h. On the basis of these results above, we propose the rational formation mechanism of BiOCl/Bi₂S₃ involving the selective ion-exchange reaction of BiOCl nanoplates, the following

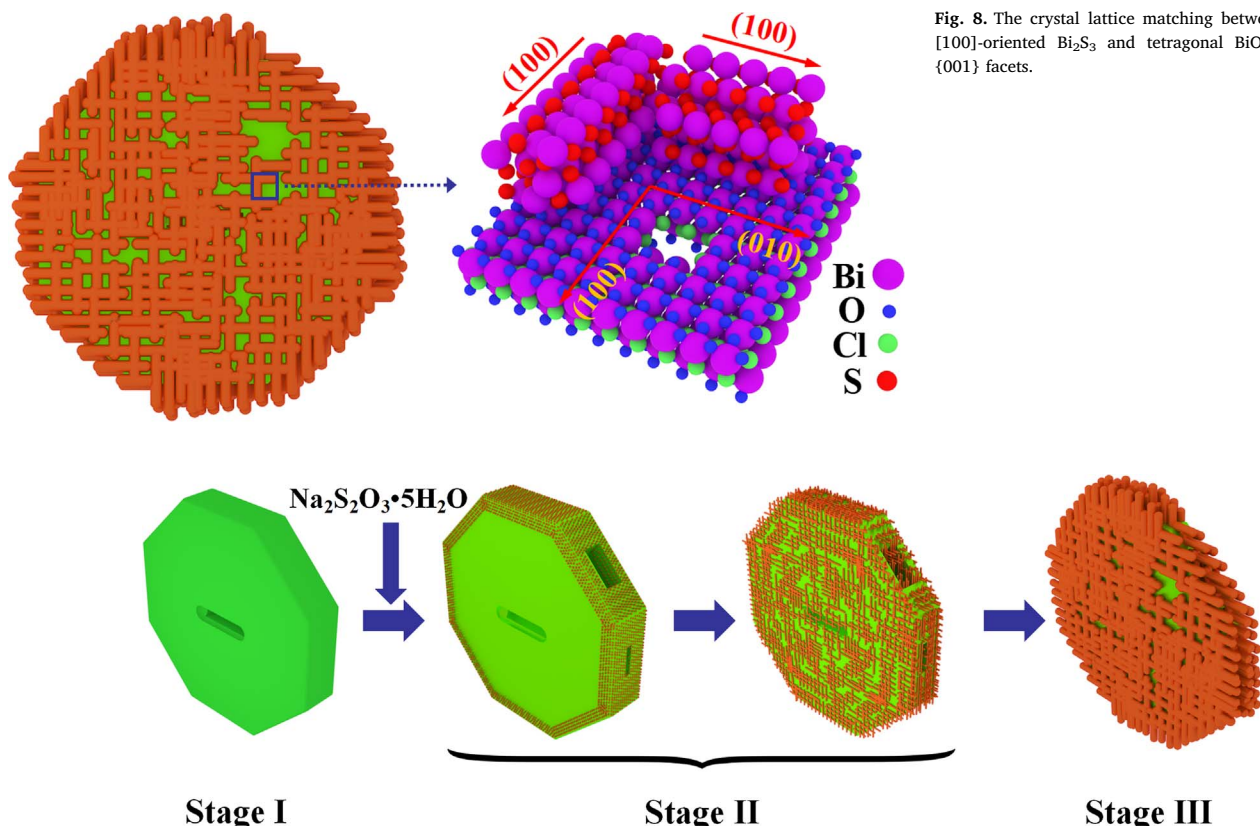


Fig. 8. The crystal lattice matching between orthorhombic [100]-oriented Bi_2S_3 and tetragonal BiOCl with exposed $\{001\}$ facets.

Scheme 1. The proposed formation mechanism of the hierarchical $\text{BiOCl}/2\text{D}$ networks Bi_2S_3 heterostructures: stage I, the precursor BiOCl irregular octagonal nanoplates; stage II, selective ion-exchange process; stage III, the following Ostwald ripening process and epitaxial growth.

Ostwald ripening process and epitaxial growth as displayed in **Scheme 1**.

3.4. Optical and electrochemical properties

The UV-visible diffuse reflectance spectra of the phase-pure BiOCl and $\text{BiOCl}/\text{Bi}_2\text{S}_3$ samples were measured to determine their light

absorption characteristics. As shown in **Fig. 9a**, pure BiOCl exhibited a strong absorption at wavelengths lower than about 370 nm, implying a photo-response at ultraviolet region. While $\text{BiOCl}/\text{Bi}_2\text{S}_3$ samples show strong photo absorption range from 200 to 1000 nm, indicating stronger visible light absorption ability than pure BiOCl . Benefiting from the introduction of S^{2-} ions and the porous structure, the 3D hierarchical $\text{BiOCl}/\text{Bi}_2\text{S}_3$ heterostructures have the extended light

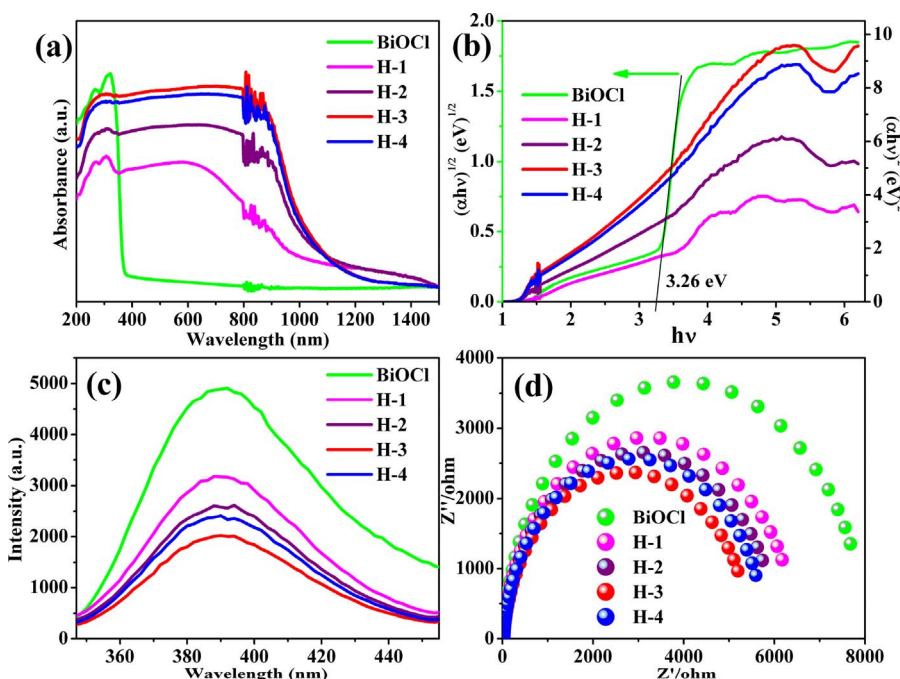


Fig. 9. (a) UV-vis diffuse reflectance spectra (DRS), (b) Bandgap energies, (c) Photoluminescence spectra (excited by 240 nm), (d) EIS Nyquist plots of pure BiOCl and different $\text{BiOCl}/\text{Bi}_2\text{S}_3$ samples.

absorbance range compared to phase-pure BiOCl, which may be benefit for photocatalytic reaction.

Generally, the optical absorption property of photocatalyst is often closely associated with its energy gap. The energies of the band gap of as-obtained samples could be estimated by extrapolating the straight portion of plot to $\alpha = 0$ based on the formula [57]:

$$\alpha h\nu = A(h\nu - E_g)^n/2 \quad (1)$$

where α , h , ν , E_g , and A are absorption coefficient, Planck constant, light frequency, band gap, and a constant, respectively. And n is determined from the characteristic of optical transition of a semiconductor, where $n = 1$ for direct transition and $n = 4$ for indirect transition. For Bi_2S_3 , the value of n is 1 for the direct transition, while $n = 4$ for BiOCl. By extrapolating the linear portion of the $(\alpha h\nu)^2$ versus $h\nu$ curves (Fig. 9b) to the energy axis at $\alpha = 0$, the band gaps of the BiOCl/ Bi_2S_3 samples (H-1, H-2, H-3, H-4) are estimated to be 1.29 eV, 1.27 eV, 1.26 eV, 1.26 eV, (Fig. S5a) which are between the pure BiOCl (3.26 eV) [39,40] and pure Bi_2S_3 1.26 eV (Fig. S5).

To test the recombination rate of photogenerated electrons and holes, room-temperature steady-state photoluminescence spectra of obtained samples were also employed. As shown in Fig. 9c, all samples exhibited broad emission peaks around 350–450 nm. Obviously, all BiOCl/ Bi_2S_3 samples display weakened PL intensity compared with the pure BiOCl. Interestingly, with the more addition of $\text{Na}_2\text{S}_2\text{O}_3 \cdot 5\text{H}_2\text{O}$, the BiOCl/ Bi_2S_3 sample H-4 shows higher PL intensity than H-3, which was possibly attributed to excessive Bi_2S_3 possessing poor transport and high recombination rate of photoinduced carriers [59]. The BiOCl/ Bi_2S_3 sample H-3 shows the lowest photoluminescence intensity, indicating the lowest recombination rate of photoinduced carriers. It may be attributed to the formation of heterojunctions between BiOCl and Bi_2S_3 , the appropriate introduction amount of S^{2-} ions and the porous structure [16].

In addition, to further investigate the separation and transfer efficiency of photogenerated electron-hole pairs, the electrochemical impedance spectra (EIS) of phase-pure BiOCl and BiOCl/ Bi_2S_3 composites was employed. The smaller arc radius implies a higher efficiency of charge transfer [55]. As shown in Fig. 9d, the H-3 samples possessed the smallest arc radius of the Nyquist plots, implying the optimal separation and transfer of photoinduced carriers. The proper introduction content of Bi_2S_3 phase may be responsible for the enhanced performance.

Combined with these results, the formation of heterostructures between BiOCl and Bi_2S_3 and the porous structure made the BiOCl/ Bi_2S_3 composites possess extended photo-responsive range, lower recombination rate of photoinduced carriers and enhanced interfacial charge separation and transfer ability.

3.5. Photoreactivity driven by visible light

To demonstrate the photocatalytic activity of as-obtained samples, photocatalytic reduction of Cr^{VI} by the as-obtained pure BiOCl and various BiOCl/ Bi_2S_3 heterostructures samples under visible-light irradiation is investigated as shown in Fig. 10a. As contrast, pure Bi_2S_3 obtained after 48 h of ion-exchange, physical mixture of pure BiOCl and pure Bi_2S_3 (mass ratio = 1:1) were also used to conduct photocatalytic reduction of Cr^{VI} . As we can see, the self-photo-degradation of Cr^{VI} was almost negligible, indicating that the good structural stability of Cr^{VI} . After irradiation for 2 h, the sample H-3 exhibits the highest photocatalytic activity with 84.9% of Cr^{VI} reduction (Fig. 10b), which was higher than 2.95%, 58.3%, 55.4%, 37.3%, 65.3%, 79.0% of reduction in pure BiOCl, pure Bi_2S_3 , the mixture, H-1, H-2, H-4, respectively. Furthermore, the samples H-2, H-3, H-4 exhibit significantly higher photocatalytic activity than those of pure BiOCl, pure Bi_2S_3 , and physical mixture of pure BiOCl and pure Bi_2S_3 .

In addition, the linear relationship between $-\ln(C/C_0)$ and reaction time (t) was investigated, which suggested that the Cr^{VI} reduction

reaction was fitted well with pseudo-first-order kinetics model.

$$-\ln(C/C_0) = kt \quad (2)$$

where C is the concentration of the Cr^{VI} at time t , C_0 is the initial concentration of the Cr^{VI} solution, and the slope k is the apparent reaction rate constant [57]. As shown in Fig. 10c, the apparent reaction rate constant of sample H-3 is 0.01078 min^{-1} , which is 1.1 times that of H-4 ($k = 0.00937 \text{ min}^{-1}$), 1.9 times that of H-2 ($k = 0.00567 \text{ min}^{-1}$), 3.4 times that of H-1 ($k = 0.00332 \text{ min}^{-1}$), 107.8 times that of pure BiOCl ($k = 1.00681 \times 10^{-4} \text{ min}^{-1}$), 5.3 times that of Bi_2S_3 ($k = 0.00205 \text{ min}^{-1}$), 6.0 times that of physical mixture of pure BiOCl and pure Bi_2S_3 ($k = 0.00179 \text{ min}^{-1}$). Thus we can conclude that the sample H-3 possesses the best photocatalytic ability for Cr^{VI} reduction. We also analysed the photocatalytic ability for reduction of Cr^{VI} after eliminating the adsorption. As shown in Fig. S6, the sample H-3 exhibits the best photocatalytic performance for 76.88% Cr^{VI} reduction in 2 h. And it is obvious that all the BiOCl/ Bi_2S_3 heterostructures samples show better photocatalytic activities than pure BiOCl, pure Bi_2S_3 , and the mixture.

It is nonnegligible that the surface oxygen state plays a very important role for the performance of the photocatalysts. The catalysts of metallic Ni modified by surface oxides showed excellent performance for CO hydrogenation reaction under visible light [60]. Monolayer NiTi layered double hydroxide (NiTi-LDH) nanosheets with Ni^{3+} sites formed by oxygen vacancy defects exhibited excellent electrochemical capacitive performance [61]. The (001) and (010) surfaces of BiOCl have specific structures of oxygen vacancies, which could activate adsorbed water toward improved water oxidation [62]. In our case, we confirmed the existence of oxygen vacancies, which generated at the first hydrothermal reaction in pure BiOCl and became more at the ion-exchange reaction in BiOCl/ Bi_2S_3 . The oxygen vacancies can facilitate the charge-transfer and improve the photocatalytic performance by serving as adsorption and active electron trap sites [43,63].

The formation of the heterostructures, the suitable introduction amount of Bi_2S_3 phase in BiOCl/ Bi_2S_3 composites, the special spatial structure and the oxygen vacancies are responsible for the enhanced photocatalytic activity.

3.6. Photocatalytic mechanisms

To give more definite insights into the photocatalysis mechanism, the valence band (VB) position and the conduction band (CB) position at the point of zero charge can be theoretically predicted by the following empirical formula [64] using Mulliken electronegativity definition:

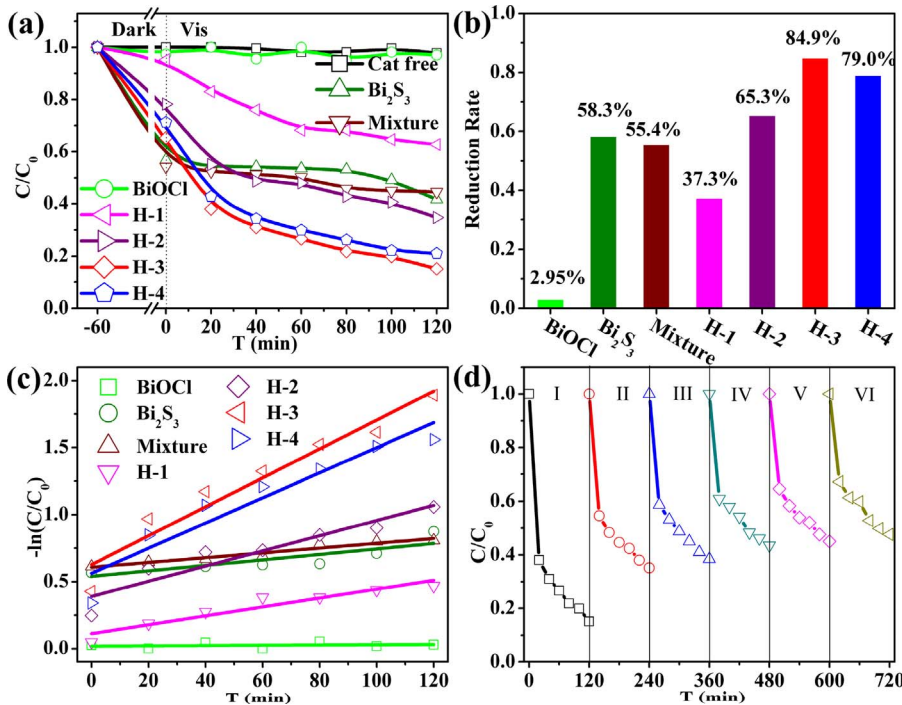
$$E_{\text{VB}} = X - E_e + 1/2E_g \quad (3)$$

$$E_{\text{CB}} = E_{\text{VB}} - E_g \quad (4)$$

where E_{VB} is the valence band (VB) edge potential, X is the absolute electronegativity of the semiconductor, which is defined as the geometric mean of the absolute electronegativity of the constituent atoms, E_e is the energy of free electrons on the hydrogen scale (ca. 4.5 eV), E_g is the band gap of the semiconductor, and E_{CB} the conduction band (VB) edge potential.

According to the literature [41,23,24], the values of X are 6.36 eV, 5.27 eV for BiOCl, Bi_2S_3 , respectively. Therefore, the E_{VB} and E_{CB} values of phase-pure BiOCl were reasonably calculated about 3.52 eV and 0.26 eV, respectively. The E_{VB} and E_{CB} values of pure Bi_2S_3 were calculated about 1.44 eV and 0.18 eV, respectively (Table S3).

According to the related calculations about band energy, the potentials of conduction band (CB) of Bi_2S_3 are more negative than that of BiOCl. Based on the band gap structure of BiOCl/ Bi_2S_3 as well as the effects of oxygen vacancies, a possible pathway for the photocatalytic reduction of Cr^{VI} was proposed as Fig. S7. Under visible-light ($\lambda > 420 \text{ nm}$) irradiation, Bi_2S_3 with narrow E_g will be activated while



BiOCl will be not. Photogenerated electrons in the CB of Bi₂S₃ transfer to the CB of BiOCl, while the holes stay on the VB of Bi₂S₃ and then react with components adsorbed on the surface of BiOCl/Bi₂S₃. The photogenerated electrons in the CB of BiOCl are partially captured by oxygen vacancies, which is in favor of the separation and transfer of photogenerated carriers. The photogenerated electrons in the CB of BiOCl and captured by oxygen vacancies are responsible for the photocatalytic reduction of Cr^{VI}.

3.7. Reusability and stability

To further investigate the reusability and stability of the as-prepared BiOCl/Bi₂S₃ heterostructures (sample H-3), we collect and reuse the same photocatalyst for 6 cycles (Fig. 10d). After the first photocatalytic measurement, the photocatalytic activity decreased to some degree, which might be partly caused by minor damage of the photocatalyst architecture (Fig. S8). Only insignificant loss in photocatalytic activity is observed in the continuing measurement, which might be partly caused by incomplete collection of the photocatalyst during each step [16]. As shown in Fig. S9, the XRD pattern of sample H-3 after the photocatalytic measurement reveals almost no deterioration in the crystal structure, indicating the good stability.

4. Conclusion

In summary, we have successfully synthesized uniform, porous and hierarchical BiOCl/2D networks Bi₂S₃ heterostructures by a facile two-step hydrothermal method, which includes an ion-exchange process between precursor BiOCl irregular octagonal nanoplates and Na₂S₂O₃·5H₂O in an aqueous solution. The transformation mechanism from BiOCl nanoplates into porous BiOCl/Bi₂S₃ composites seems to involve the selective ion-exchange of BiOCl nanoplates, the subsequent Ostwald ripening process and epitaxial growth. And the crystal lattice matching between the a- or b-axis of tetragonal BiOCl ($a = b = 3.89 \text{ \AA}$) and the a-axis of orthorhombic Bi₂S₃ ($a = 3.981 \text{ \AA}$) could be responsible for the topotactic transformation. We also found that the as-obtained BiOCl/Bi₂S₃ hybrids exhibited enhanced photocatalytic activity for reduction of Cr^{VI} under visible-light illumination. The formation of the heterostructures, the suitable introduction amount of

Fig. 10. (a) Reduction curves of Cr(VI) under visible light radiation catalyzed by different samples, (b) The corresponding reduction rate of Cr(VI) under radiation for 2 h, (c) $-\ln(C/C_0)$ versus time curves, (d) 6 recycled runs of photocatalytic reduction of Cr(VI) using the sample H-3 as the catalyst.

Bi₂S₃ phase, the distinctive porous spatial architecture and the presence of oxygen vacancies are responsible for the enhanced photocatalytic activity. Our synthesis strategy of the 3D porous heterojunctions are expected to inspire further attempts for the fundamental investigation on shape-dependent improved performances for various promising applications.

Acknowledgement

This work was supported by Natural Science Foundation of China (21673300) and Fundamental Research Funds for the Central Universities, South-central University for Nationalities (CZP17039).

Appendix A. Supplementary data

Supplementary data associated with this article can be found, in the online version, at <http://dx.doi.org/10.1016/j.apcatb.2017.08.074>.

References

- [1] P.V. Kamat, J. Phys. Chem. C 112 (2008) 18737–18753.
- [2] Q.L. Bao, K.P. Loh, ACS Nano 6 (2012) 3677–3694.
- [3] R. Asahi, T. Morikawa, T. Ohwaki, K. Aoki, Y. Tagai, Science 293 (2001) 269–271.
- [4] Z.W. Mao, R. Cartier, A. Hohl, M. Farinacci, A. Dorhoi, T.L. Nguyen, P. Mulvaney, J. Ralston, S.H.E. Kaufmann, H. Möhwald, D.Y. Wang, Nano Lett. 11 (2011) 2152–2156.
- [5] M. Saruyama, M. Kanehara, T. Teranishi, J. Am. Chem. Soc. 132 (2010) 3280–3282.
- [6] G.D. Moon, S. Ko, Y.N. Xia, U.Y. Jeong, ACS Nano 4 (2010) 2307–2319.
- [7] F. Wang, Y. Han, C.S. Lim, Y.H. Lu, J. Wang, J. Xu, H.Y. Chen, C. Zhang, M.H. Hong, X.G. Liu, Nature 463 (2010) 1061–1065.
- [8] R.K. Joshi, J.J. Schneider, Chem. Soc. Rev. 41 (2012) 5285–5312.
- [9] R. Houbertz, L. Fröhlich, M. Popall, U. Streppe, P. Dannberg, A. Bräuer, J. Serbin, B.N. Chichkov, Adv. Eng. Mater. 5 (2003) 551–555.
- [10] Z. Fang, K.B. Tang, G.Z. Shen, D. Chen, R. Kong, S.J. Lei, Mater. Lett. 60 (2006) 2530–2533.
- [11] H. Zhang, H. Wang, Y. Xu, S.F. Zhuo, Y.F. Yu, B. Zhang, Angew. Chem. Int. Ed. 51 (2012) 1459–1463.
- [12] Y.J. Hwang, A. Boukai, P.D. Yang, Nano Lett. 9 (2009) 410–415.
- [13] D.L. Wang, F. Qian, C. Yang, Z.H. Zhong, C.M. Lieber, Nano Lett. 4 (2004) 871–874.
- [14] A.G. Dong, R. Tang, W.E. Buhro, J. Am. Chem. Soc. 129 (2007) 12254–12262.
- [15] X.J. Wu, J. Chen, C.L. Tan, Y.H. Zhu, H. Zhang, Nat. Chem. 8 (2016) 470–475.
- [16] X.H. Gao, H.B. Wu, L.X. Zheng, Y.J. Zhong, Y. Hu, X.W. Lou, Angew. Chem. Int. Ed. 53 (2014) 5917–5921.
- [17] Y. Nonoguchi, T. Nakashima, T. Kawai, Small 5 (2009) 2403–2406.

- [18] Y. Hu, H.H. Qian, Y. Liu, G.H. Du, F.M. Zhang, L.B. Wang, X. Hu, *CrystEngComm* 13 (2011) 3438–3443.
- [19] Y. Liu, L. Yu, Y. Hu, C.F. Guo, X.W. Lou, *Nanoscale* 4 (2012) 183–187.
- [20] J.S. Chen, D.Y. Luan, C.M. Li, F.Y.C. Boey, S.Z. Qiao, *Chem. Commun.* 46 (2010) 8224–8254.
- [21] A. Forticaux, S. Hacialioğlu, J.P. DeGrave, R. Dziedzic, S. Jin, *ACS Nano* 7 (2013) 8224–8232.
- [22] L.D. Trizio, F.D. Donato, A. Casu, A. Falqui, M. Povia, L. Manna, *ACS Nano* 7 (2013) 3997–4005.
- [23] H.F. Cheng, B.B. Huang, Y. Dai, *Nanoscale* 6 (2014) 2009–2026.
- [24] L.Q. Ye, Y.R. Su, X.L. Jin, H.Q. Xie, C. Zhang, *Environ. Sci. I* (2014) 90–112.
- [25] J. Jiang, K. Zhao, X.Y. Xiao, L.Z. Zhang, *J. Am. Chem. Soc.* 134 (2012) 4473–4476.
- [26] L.Y. Ding, H. Chen, Q.Q. Wang, T.F. Zhou, Q.Q. Jiang, J.L. Li, J.C. Hu, *Chem. Commun.* 52 (2016) 994–997.
- [27] S. Bai, X.Y. Li, Q. Kong, R. Long, C.M. Wang, J. Jiang, Y.J. Xiong, *Adv. Mater.* 27 (2015) 3444–3452.
- [28] C.W. Tan, G.Q. Zhu, M. Hojamberdiev, K. Okada, J. Liang, X.C. Luo, P. Liu, *Appl. catal. B: Environ.* 152 (2014) 425–436.
- [29] G.Q. Zhu, M. Hojamberdiev, K. Katsumata, N. Matsushita, K. Okada, P. Liu, J.P. Zhou, Y. Liu, *Adv. Powder Technol.* 25 (2014) 1292–1303.
- [30] G.Q. Zhu, M. Hojamberdiev, C.W. Tan, L. Jin, C. Xu, Y. Liu, P. Liu, J.P. Zhou, *Mater. Chem. Phys.* 147 (2014) 1146–1156.
- [31] F. Teng, W.X. Ouyang, Y.M. Li, L.X. Zheng, X.S. Fang, *Small* 13 (2017).
- [32] J.M. Ma, Z.F. Liu, J.B. Lian, X.C. Duan, T. Kim, P. Peng, X.D. Liu, Q. Chen, G. Yao, W.J. Zheng, *CrystEngComm* 13 (2011) 3072–3079.
- [33] L.S. Li, N.J. Sun, Y.Y. Huang, Y. Qin, N. Zhao, J.N. Gao, M.X. Li, H.H. Zhou, L.M. Qi, *Adv. Funct. Mater.* 18 (2008) 1194–1201.
- [34] G. Konstantatos, L. Levina, J. Tang, E.H. Sargent, *Nano Lett.* 8 (2008) 4002–4006.
- [35] S. Balachandran, M. Swaminathan, *Dalton Trans.* 42 (2013) 5338–5347.
- [36] Y.F. Jiang, J.C. Hu, J.L. Li, *RSC Adv.* 6 (2016) 39810–39817.
- [37] S.H. Jiang, K.Q. Zhou, Y.Q. Shi, S.M. Lo, H.Y. Xu, Y. Hu, Z. Gui, *Appl. Surf. Sci.* 290 (2014) 313–319.
- [38] V.C. Ferreira, M.C. Neves, A.R. Hillman, O.C. Monteiro, *RSC Adv.* 6 (2016) 77329–77339.
- [39] Z.M. Jia, W. Chen, T.Y. Liu, T. Huang, X.H. Liu, *J. Wuhan Univ. Technol. Mater. Sci. Ed.* 31 (2016) 765–772.
- [40] J. Cao, B.Y. Xu, H.L. Lin, B.D. Luo, S.F. Chen, *Catal. Commun.* 26 (2012) 204–208.
- [41] H.F. Cheng, B.B. Huang, X.Y. Qin, X.Y. Zhang, Y. Dai, *Chem. Commun.* 48 (2012) 97–99.
- [42] W.L. Yang, L. Zhang, Y. Hu, Y.J. Zhong, H.B. Wu, X.W. Lou, *Angew. Chem. Int. Ed.* 51 (2012) 11501–11504.
- [43] L.Q. Ye, L. Zan, L.H. Tian, T.Y. Peng, J.J. Zhang, *Chem. Commun.* 47 (2011) 6951–6953.
- [44] C.Z. Wei, L.F. Wang, L.Y. Dang, Q. Chen, Q.Y. Lu, F. Gao, *Sci. Rep.* 5 (2015) 10599–10608.
- [45] C.F. Guo, S.H. Cao, J.M. Zhang, H.Y. Tang, S.M. Guo, Y. Tian, Q. Liu, *J. Am. Chem. Soc.* 133 (2011) 8211–8215.
- [46] C.F. Guo, J.M. Zhang, Y. Tian, Q. Liu, *ACS Nano* 6 (2012) 8746–8752.
- [47] C.F. Guo, J.M. Zhang, M. Wang, Y. Tian, Q. Liu, *Small* 9 (2013) 2394–2398.
- [48] X.F. Zhou, Z.L. Hu, Y.Q. Fan, S. Chen, W.P. Ding, N.P. Xu, *J. Phys. Chem. C* 112 (2008) 11722–11728.
- [49] M. Kruk, M. Jaroniec, *Chem. Mater.* 13 (2001) 3169–3183.
- [50] S.G. Wang, X. Li, Y. Chen, X.J. Cai, H.L. Yao, W. Gao, Y.Y. Zheng, X. An, J.L. Shi, *Adv. Mater.* 27 (2015) 2775–2782.
- [51] Y. Yu, C.Y. Cao, H. Liu, P. Li, F.F. Wei, Y. Jiang, W.Q. Song, *J. Mater. Chem. A* 2 (2014) 1677–1681.
- [52] H.P. Jiao, X. Yu, Z.Q. Liu, P.Y. Kuang, Y.M. Zhang, *RSC Adv.* 5 (2015) 16239–16249.
- [53] Z.Q. Liu, W.Y. Huang, Y.M. Zhang, Y.X. Tong, *CrystEngComm* 14 (2012) 8261–8267.
- [54] H. Wang, X.Z. Yuan, Y. Wu, G.M. Zeng, W.G. Tu, C. Sheng, Y.C. Deng, F. Chen, J.W. Chew, *Appl. Catal. B* 209 (2017) 543–553.
- [55] J. Ding, Z. Dai, F. Qin, H.P. Zhao, R. Chen, *Appl. Catal. B* 205 (2017) 281–291.
- [56] Y.Q. Lei, G.H. Wang, S.Y. Song, W.Q. Fan, H.J. Zhang, *CrystEngComm* 11 (2009) 1857–1862.
- [57] X.Y. Xiong, L.Y. Ding, Q.Q. Wang, Y.X. Li, Q.Q. Jiang, J.C. Hu, *Appl. Catal. B* 188 (2016) 283–291.
- [58] F. Tian, J.Y. Xiong, H.P. Zhao, Y.L. Liu, S.Q. Xiao, R. Chen, *CrystEngComm* 16 (2014) 4298–4305.
- [59] J. Kim, M. Kang, *Int. J. Hydrogen Energy* 37 (2012) 8249–8256.
- [60] Y.F. Zhao, B. Zhao, J.J. Liu, G.B. Chen, R. Gao, S.Y. Yao, M.Z. Li, Q.H. Zhang, L. Gu, J.L. Xie, X.D. Wen, L.Z. Wu, C.H. Tung, D. Ma, T.R. Zhang, *Angew. Chem. Int. Ed.* 55 (2016) 4215–4219.
- [61] Y.F. Zhao, Q. Wang, T. Bian, H.J. Yu, H. Fan, C. Zhou, L.Z. Wu, C.H. Tung, D.O. Hare, T.R. Zhang, *Nanoscale* 7 (2015) 7168–7173.
- [62] H. Li, J. Shang, H.J. Zhu, Z.P. Yang, Z.H. Ai, L.Z. Zhang, *ACS Catal.* 6 (2016) 8276–8285.
- [63] Y.F. Zhao, X.D. Jia, G.B. Chen, L. Shang, G.I.N. Waterhouse, L.Z. Wu, C.H. Tung, D.O. Hare, T.R. Zhang, *J. Am. Chem. Soc.* 138 (2016) 6517–6524.
- [64] Y. Xu, M.A.A. Schoonen, *Am. Mineral.* 85 (2000) 543–556.